Research Square

Preprints are preliminary reports that have not undergone peer review.
They should not be considered conclusive, used to inform clinical practice,
or referenced by the media as validated information.

Dual-Timescale Hysteresis Modeling with a Square-Root Central Difference Kalman Filter for Robust State-of-Charge Estimation of Strongly Hysteretic Lithium-Ion Batteries

Kun Wang

492839759@qq.com

Yancheng Polytechnic College of Industry Technology

Research Article

Keywords: State of charge, Equivalent circuit model, Voltage hysteresis, Square-root central difference Kalman filter, Lithium-rich manganese oxide, LiFePO4

Posted Date: November 11th, 2026

DOI: https://doi.org/10.21203/rs.3.rs-11685961/v1

License: This work is licensed under a Creative Commons Attribution 4.0 International License.
Read Full License

Additional Declarations: No competing interests reported.

Dual-Timescale Hysteresis Modeling with a Square-Root Central Difference Kalman Filter for Robust State-of-Charge Estimation of Strongly Hysteretic Lithium-Ion Batteries

Kun Wang

School of Automotive and Transportation, Yancheng Polytechnic College of Industry Technology, Yancheng 224005, Jiangsu, China

Corresponding author: 492839759@qq.com

Abstract

Accurate state-of-charge (SOC) estimation is essential to the battery management system but becomes difficult when the open-circuit voltage (OCV) is strongly path dependent, as in lithium-rich and conversion-type chemistries, or almost flat, as in LiFePO4. This study couples a second-order equivalent circuit model with a dual-timescale hysteresis description—a fast, current-weighted direction state plus a slow random-walk magnitude state that absorbs ageing- and temperature-induced drift—and recovers the state by a square-root central difference Kalman filter (SRCDKF) whose deterministic sigma points and QR covariance propagation remain well conditioned where the OCV slope is near zero. Three evidence levels are used. Genuine 0.1C galvanostatic curves of a lithium-rich/MnO@C coin cell give a mean hysteresis width of 0.457 V, and a 0.1C/1C rate gap anchors the ohmic-resistance order (about 18.5 ohm for a 2 mAh cell). A labeled synthetic test shows that under a +30% magnitude mismatch the proposed filter holds 0.58% SOC error whereas fixed-magnitude and extended Kalman (EKF) baselines diverge. On public CALCE data it reaches 1.01% mean error over six unseen NMC profiles and 0.40–2.16% over A123 LiFePO4 profiles at 0, 25 and 50 °C, against 3.70% and 4.85–12.49% (worst case 20.63%) for a same-model EKF. A Monte-Carlo study shows this ranking to be invariant to ±50% errors in the representative RC parameters, while capacity must be measured independently. At 0.3–0.4 ms per step the estimator is real-time feasible.

Keywords: State of charge; Equivalent circuit model; Voltage hysteresis; Square-root central difference Kalman filter; Lithium-rich manganese oxide; LiFePO4

1. Introduction

1.1 Background and motivation

Reliable knowledge of the state of charge (SOC), the fraction of the available capacity that remains in a cell, underpins almost every function of an electric-vehicle battery management system, from range prediction and charge control to cell balancing and fault diagnosis. Because SOC cannot be measured directly, it must be inferred from current and voltage, and the quality of that inference is bounded by how faithfully the battery model represents the cell and by how robustly the estimator tolerates model mismatch,

uncertain initialization and measurement noise [1,2]. Among the available approaches, equivalent circuit models (ECMs) coupled with a state observer remain the dominant practical choice: they capture the dominant voltage dynamics with a small number of physically interpretable parameters, impose a modest computational burden, and avoid the large training data sets and poor extrapolation that constrain purely data-driven estimators [3,4].

Within the model-based family, the choice of circuit order and the choice of observer are the two principal design decisions. A systematic comparison of eleven ECM topologies showed that the first- and second-order RC networks offer the best compromise between accuracy and numerical reliability for lithium-ion cells, that increasing the RC order beyond two does not consistently improve SOC accuracy and can introduce over-fitting, and—critically for the present work—that an accurate OCV–SOC characterization is indispensable regardless of the network that is adopted [3]. A broader systematic review of lumped-parameter models reached the same conclusion and further demonstrated, on both LiNMC and LiFePO4 cells, that a hysteresis branch is necessary whenever the charge and discharge OCV curves do not coincide [5]. For the observer, the extended Kalman filter (EKF) is the classical solution [6], but its first-order linearization introduces bias when the cell is nonlinear and can become ill-conditioned when the local OCV slope is small. Sigma-point filters, which propagate a deterministic set of sample points through the nonlinear model, avoid analytical Jacobians and generally improve robustness; the square-root variants additionally propagate the Cholesky factor of the covariance rather than the covariance itself, which guarantees symmetry and positive-definiteness in finite precision [7–9].

1.2 The strong-hysteresis problem

The standard ECM–observer pipeline presumes that OCV is a single-valued, reasonably steep function of SOC. That presumption fails for an increasingly important class of high-energy chemistries. In lithium- and manganese-rich layered oxide cathodes, reversible anionic (oxygen) redox contributes a large fraction of the capacity, but the anionic process is kinetically sluggish relative to the fast cationic redox and exhibits different oxidation and reduction potentials, which is the microscopic origin of the pronounced voltage hysteresis, voltage fade and slow relaxation characteristic of these materials [10]. Hysteresis in lithium-rich cathodes is further linked to collective transition-metal migration and metastable structural rearrangements, and it can exceed one volt in the most strongly affected compositions [11]. Conversion-type transition-metal oxide anodes show the analogous behaviour at low potential: even as the current tends to zero, a significant charge/discharge voltage separation remains because the conversion and interfacial storage reactions are intrinsically path dependent, and for MnO this quasi-static separation is of the order of tenths of a volt [12,19]. A lithium-ion cell that pairs a lithium-rich cathode with a MnO-based conversion anode therefore concentrates two hysteresis sources in one device and constitutes a demanding, strongly hysteretic test case for any SOC estimator.

The classical way to represent this behaviour inside an ECM is the Plett hysteresis state, a dimensionless variable driven by current that relaxes toward +1 or −1 according to the direction of charge or discharge

[6]. This formulation describes the *direction* of the branch efficiently, but it treats the hysteresis *magnitude* as a fixed, SOC-dependent map identified in advance. In a real cell the effective magnitude drifts slowly with temperature, ageing and unit-to-unit spread, and a fixed map becomes a source of bias that the direction state cannot remove. Recent physically motivated and temperature-adaptive hysteresis models confirm that magnitude is neither constant nor purely a function of SOC, but they achieve fidelity at a parameterization cost that is difficult to meet when only simple galvanostatic tests are available [13,14]. A separate difficulty appears at the other end of the spectrum: in LiFePO4 the OCV is not strongly hysteretic in the present sense but is extremely flat over a wide SOC interval, so the measurement Jacobian dOCV/dz approaches zero, the voltage carries almost no local SOC information, and a Jacobian-based EKF can lose its correction gain and fail to recover from an initial error [5,15]. A practically useful estimator should therefore handle a large, slowly varying hysteresis on one chemistry and a near-unobservable voltage plateau on another, using the same algorithmic structure.

1.3 Gap and contributions

Square-root central difference filters have been applied to lithium-ion SOC estimation, and their superior numerical stability relative to the EKF is documented [8,9], as are comparative studies of EKF, UKF and particle filters under dynamic loads [15] and joint parameter/state estimators that adapt an otherwise fixed model [16]. To the author's knowledge, however, existing sigma-point SOC studies are demonstrated almost exclusively on conventional, weakly hysteretic chemistries whose parameters are fully identified from an HPPC test, at a single temperature and on a single chemistry. Three questions remain open. First, how should hysteresis be modeled so that both its fast branch direction and its slow magnitude drift are represented without a costly parameterization campaign? Second, is the numerical advantage of a square-root sigma-point filter decisive specifically where voltage observability is weak, namely on a flat OCV plateau? Third, how sensitive is the comparison to power parameters that cannot be measured when only low-rate galvanostatic data are available?

This work addresses these questions and makes the following contributions.

1. A dual-timescale hysteresis ECM is proposed, in which a fast Plett-type direction state is augmented with a slow random-walk magnitude-correction state; the two operate on deliberately separated time scales and the slow state absorbs drift without flipping sign at each current reversal.

2. The model is embedded in an SRCDKF that propagates covariance through QR decomposition of a weighted sigma-point matrix, preserving positive-definiteness without an analytical Jacobian, and three ablations (fixed magnitude, no hysteresis, same-model EKF) isolate the origin of every gain.

3. A three-level, fully traceable evidence chain is built without fabricating dynamic experiments that were not performed: genuine low-rate coin-cell curves supply the intrinsic OCV, hysteresis and the ohmic-resistance order; a clearly labeled synthetic test isolates mechanism; and two independent public CALCE chemistries (sloped-OCV NMC and flat-OCV LiFePO4, the latter at three temperatures) supply out-of-sample dynamic validation.

4. A Monte-Carlo sensitivity analysis quantifies the dependence of the method ranking on the representative RC parameters and on capacity, giving an explicit and honest statement of which parameters must be measured precisely.

The remainder of the paper presents the model and filter (Section 2), the data sources and parameterization (Section 3), the results (Section 4), a discussion of mechanism, scope and limitations (Section 5), and conclusions (Section 6).

2. Model and estimation method

2.1 Second-order ECM with dual-timescale hysteresis

A second-order RC network is used because it balances voltage-fidelity against parameter reliability [3]. Let z denote SOC, $U1$ and $U2$ the polarization voltages of a fast and a slow RC branch, I the current (positive on discharge), and t time. With an ohmic resistance $R0$, branch resistances $R1$, $R2$ and time constants $\tau 1$, $\tau 2$, the continuous dynamics are discretized at step dt by analytic integration, which is unconditionally stable for any dt:

$$(1)\quad z_{k+1} = z_k - \eta\, I_k\, dt / Q_s\,,$$

$$(2)\quad U_{i,k+1} = U_{i,k}\, \exp(-dt/\tau_i) + R_i\, I_k\, [1 - \exp(-dt/\tau_i)],\quad i = 1, 2,$$

where Q_s = 3600 Q is the cell capacity in ampere-seconds and η is coulombic efficiency. The terminal-voltage measurement is

$$(3)\quad V_k = OCV(z_k) - U1,k - U2,k + U_h,k - R0\, I_k + v_k\,,$$

in which $OCV(z)$ is the single-valued mid-OCV obtained by averaging the charge and discharge curves and U_h is the hysteresis contribution.

The hysteresis term is written as

$$(4)\quad U_h,k = [\, M(z_k) + m_{d,k}\,]\, h_k\,,$$

where $M(z)$ is the SOC-dependent half-width identified from the genuine charge/discharge separation, h is the fast direction state and m_d is the slow magnitude correction. The direction state follows the current-weighted relaxation introduced by Plett [6]:

$$(5)\quad h_{k+1} = h + (h_k - h)\, \exp(-K_F\, |I_k|\, dt),\quad h^* = -\mathrm{sign}(I_k),$$

with the gain K_F chosen so that the branch is forgotten over a prescribed small throughput (here two percent of capacity); when the current is zero, h is held. Equation (5) tracks which branch the cell occupies on a time scale of a few percent of capacity. In contrast, m_d is modeled as a zero-mean random walk,

$$(6)\quad m_{d,k+1} = m_{d,k} + w_{d,k},$$

whose process noise is several orders of magnitude smaller than that of h, so that m_d evolves only over a large throughput and estimates the slow, sign-preserving offset between the nominal map $M(z)$ and the hysteresis magnitude that the cell actually exhibits. Crucially, m_d does not reverse when the current

reverses; it is the slowly varying *amplitude* error, whereas *h* carries the fast *direction*. This separation is the principal modeling distinction from a conventional single hysteresis state, which conflates the two.

Three ablations are used throughout to attribute the observed gains. The **fixed-magnitude** filter retains *h* but sets $m_d \equiv 0$, reducing Eq. (4) to the classical Plett form; the **no-hysteresis** filter sets $h = m_d = 0$ and relies on the mid-OCV alone; and the **EKF** uses the identical dual-timescale model but a first-order Jacobian update, so that the value of the sigma-point square-root machinery is separated from the value of the hysteresis model itself.

2.2 Square-root central difference Kalman filter

The augmented state is **x** = [z, U1, U2, h, m_d]^T, giving a five-dimensional nonlinear state-space system formed by Eqs. (1)–(6) and the measurement Eq. (3). Rather than linearize it, the central difference transform generates 2n+1 deterministic sigma points from the Cholesky factor *S* of the state covariance, with a central-difference interval $h^2 = 3$, propagates them through the nonlinear functions, and recovers the predicted mean, the predicted covariance and the cross-covariance by weighted regression [7,8]. Following the square-root formulation, the predicted Cholesky factor is obtained by a QR decomposition of the matrix that stacks the weighted, centred propagated sigma points and the Cholesky factor of the process noise; the measurement update then downdates this factor using the innovation covariance. Because a Cholesky factor is maintained at every step, the state covariance cannot lose symmetry or positive-definiteness through round-off—a failure mode to which a Riccati-recursion EKF is exposed when, as on a flat OCV plateau, the measurement is only weakly informative. No analytical Jacobian is required, removing a source of linearization bias. The same-model EKF used as a baseline computes numerical Jacobians by central finite differences with a fixed perturbation and applies the standard predict/update recursion.

2.3 Parameter identification from a single dynamic schedule

To keep the parameterization demand compatible with sparse data, parameters are identified from one dynamic schedule and all other schedules are reserved for validation. On each 1-Hz dynamic schedule, the instantaneous ohmic resistance *R0* is estimated as the median of $-\Delta V/\Delta I$ over the abrupt current steps, where only the voltage jump within the first sampling interval is used so that slow RC polarization is excluded. The mid-OCV curve is obtained by binning SOC and regressing terminal voltage on current within each bin; the intercept at zero current is a quasi-static OCV, and this bin-wise regression makes the identification insensitive to misalignment between separate tests. The RC parameters are then selected on a fixed grid of positive time constants by non-negative least-squares fit to the residual after the ohmic and OCV contributions are removed; non-negativity is imposed to avoid the unphysical negative resistances that an unconstrained global fit produces on a flat OCV curve. Capacity is not fitted by the observer: it is obtained independently, from the measured reversible capacity for the coin cell and from net coulomb counting between the fully charged and depleted endpoints for the public cells, because (as Section 4.4 shows) an unbiased capacity reference is the one quantity the filter cannot supply for itself.

3. Materials and data sources

The validation deliberately combines three evidence levels of different nature, so that no claim is supported by a single simulation and no dynamic experiment that was not physically performed is presented as measured. Genuine low-rate coin-cell curves characterize the intrinsic material behaviour; a labeled synthetic test isolates the estimator mechanism; and public dynamic data sets of two commercial chemistries provide out-of-sample validation under realistic automotive schedules.

3.1 Genuine strongly hysteretic coin-cell data

The strongly hysteretic case is a CR2032 coin cell pairing a lithium- and manganese-rich layered oxide cathode with a carbon-coated manganese-monoxide conversion anode (MnO@C), together with the corresponding cathode and anode half-cells against lithium. Galvanostatic charge/discharge (GCD) was conducted at low rate: the full cell and both half-cells at 0.1C for the first three cycles, and the cathode additionally at 1C. At such low rate, GCD is the standard experimental approximation to a quasi-static OCV measurement, so these curves are an appropriate source for the intrinsic OCV and hysteresis. The full cell delivered a reversible specific capacity of 145 mAh/g; the cathode delivered about 285 mAh/g at 0.1C and 233 mAh/g at 1C.

The printed GCD curves were digitized at high resolution. After axis registration, the stable second and third cycles were separated by colour and, for each capacity column, the upper and lower traces were extracted by a two-cluster separation that discards columns containing only a single branch (an end-of-curve artefact); the charge and discharge branches were then joined at their common crossing point. Sampling the result onto a uniform SOC grid yielded 95 points for the full cell. The digitized mid-OCV spans 2.512–3.931 V over SOC 0.03–0.97, and the full charge/discharge hysteresis width averages 0.457 V (median 0.481 V), corresponding to a half-width M of about 0.228 V. The electrode-resolved curves attribute most of this separation to the conversion anode, whose half-width averages 0.763 V over the common SOC interval (0.15–0.85, where both electrodes are defined), while the lithium-rich cathode contributes 0.219 V through its anionic-redox plateau; over this interval this corresponds to roughly 78% anode and 22% cathode contribution. It is worth stating explicitly that the sum of the two isolated-electrode half-widths (0.982 V) is an upper bound and is not forced to equal the full-cell width measured over the same interval (0.484 V; the mean over the full 0.03–0.97 SOC range is 0.457 V), because electrode matching and polarization in the assembled cell do not add linearly; the model uses the measured full-cell map rather than the electrode sum.

To anchor the otherwise representative ohmic resistance without an HPPC test, the cathode 0.1C and 1C curves were compared as a two-rate DC internal resistance (DCIR). Over the reliable mid-SOC window of 0.25–0.75, the 1C discharge curve lies 33 mV below the 0.1C curve and the charge curve 319 mV above it; with a rate difference $\Delta I = 0.2565$ A/g this gives a discharge DCIR of 0.130 Ω·g and a charge DCIR of 1.243 Ω·g. The strong charge/discharge asymmetry is consistent with sluggish anionic activation on charge reported for lithium-rich cathodes [10]. Scaled by the active cathode mass of a 2 mAh coin cell (0.0070 g at

0.285 Ah/g), the discharge DCIR is 18.5 Ω, which anchors the model value R0 = 20 Ω; the larger charge value (177 Ω) indicates why the total polarization resistance, which also includes the slow conversion anode, is of the order of tens of ohms. These cells provide only low-rate, quasi-static data; no dynamic schedule or HPPC test was performed on them, which is precisely why their power parameters are treated as representative and their influence is quantified in Section 4.4.

3.2 Public dynamic data of two commercial chemistries

Dynamic validation uses the University of Maryland CALCE battery data [17,18]. Two chemistries with contrasting OCV shapes are used. The first is a cylindrical INR18650 NMC cell with a normally sloped OCV; the dynamic stress test (DST) is used for identification and the federal urban driving schedule (FUDS), the US06 highway schedule and the Beijing dynamic stress test (BJDST), each started from both 80% and 50% initial SOC, form six profiles that are never used for fitting. Identification on DST gives R0 = 0.0717 Ω (the median over 236 abrupt current steps), R1 = 0.0168 Ω, R2 = 0.0004 Ω, $\tau1$ = 8 s, $\tau2$ = 40 s and Q = 2.0 Ah, with a DST voltage-reconstruction RMSE of 28.5 mV.

The second chemistry is an A123 26650 LiFePO4 (LFP) cell, chosen because its OCV is almost flat over most of the SOC range and it carries a small but genuine charge/discharge separation, making it the most demanding numerical-robustness case. Data at 0, 25 and 50 °C are used, with DST identified separately at each temperature and US06/FUDS reserved for validation. At 25 °C the self-consistent capacity is 1.036 Ah and R0 = 0.157 Ω; the genuine charge/discharge half-width is only 25–32 mV and is already absorbed into the discharge quasi-static OCV obtained by the bin-wise regression, so an explicit hysteresis gain is set to zero for this chemistry rather than tuned to manufacture an advantage. This choice is reported deliberately: hysteresis handling is configured according to the chemistry, and a small, already-absorbed separation should not be double counted. The DST reconstruction RMSE is 35.9 mV.

3.3 Labeled synthetic closed-loop test

Because the coin cells lack a dynamic schedule, a synthetic asymmetric-pulse profile (1.2C discharge / 0.6C charge pulses separated by rests, discharging from 90% to 45% SOC) is used solely to isolate estimator behaviour under controlled, known truth. The initial estimator SOC is offset by 20 percentage points, measurement noise is 5 mV RMS and current noise 0.5%, and every result is averaged over ten noise realizations. Two scenarios are reported: a nominal case in which the true hysteresis magnitude matches the map, and a drift case in which the magnitude grows by an unknown constant 30%, emulating slow ageing/temperature mismatch that the slow state m_d must compensate. This test is a simulation and is labeled as such throughout; it does not substitute for the measured public-data validation.

4. Results

4.1 Intrinsic OCV and hysteresis of the strong-hysteresis cell

Figure 1 shows the digitized charge/discharge and mid-OCV curves of the full cell and the electrode-resolved decomposition. A separation persists across the entire SOC window and is not a transient

polarization artefact, because it remains at the 0.1C quasi-static limit; its 0.457 V mean width is an order of magnitude larger than the few-tens-of-millivolt separation of conventional intercalation chemistries and is comparable to the strong-hysteresis behaviour reported for oxygen-redox cathodes and conversion anodes [10,12]. The decomposition in Figure 1b localizes the dominant contribution at the MnO@C conversion anode, in agreement with the path-dependent conversion/interfacial mechanism that leaves a residual voltage difference even as current approaches zero [19]. These curves establish, from measured data rather than assumption, that a single-valued OCV would carry a systematic branch-dependent bias of 0.46 V on average and up to 0.51 V in this cell, and they supply the *M(z)* map used by the estimator.

4.2 Model reconstruction and resistance anchoring

Figure 2 summarizes the open-loop model checks. Before closing the estimation loop, the analytic dual-timescale ECM was driven open loop by the measured 0.1C current; it reconstructs both the charge and discharge curves with an RMSE of 15.0 mV (Figure 2a), and on the model evaluation grid the hysteresis gap it reproduces (0.492 V) matches the corresponding measured gap on that grid (0.462 V; the full-SOC mean width is 0.457 V) within 30 mV, confirming that analytic integration and the identified map are self-consistent. The reversal and rest self-checks in Figure 2b,c further confirm the expected time-scale separation: the fast direction state responds within a few percent of throughput while the slow state remains nearly stationary over a single partial discharge and moves only over the long horizon, whereas during rest the RC polarization decays while the hysteresis voltage is held. The two-rate DCIR analysis (Figure 1c) independently places the coin-cell ohmic resistance at about 18.5 Ω on discharge, in close agreement with the adopted R0 = 20 Ω; the model's resistance scale is therefore order-anchored by measurement rather than chosen arbitrarily.

4.3 Synthetic closed-loop performance

Table 1 reports the converged SOC RMSE on the labeled synthetic profile, and Figure 3 shows the corresponding time-domain trajectories under the drift scenario. Under nominal conditions all filters are accurate, although the no-hysteresis filter already shows a 1.52% error because it cannot represent the branch; the proposed dual-timescale filter reaches 0.19% and converges in about 201 s. Under the +30% magnitude drift the distinction becomes decisive: the proposed filter holds 0.58% RMSE, whereas the fixed-magnitude filter degrades to 2.47% and never re-enters the ±2% band, the no-hysteresis filter reaches 2.79%, and the same-model EKF reaches 3.71% with a large realization-to-realization spread (±1.20%) and likewise fails to converge. The slow state *m_d* tracks the unknown magnitude offset and removes precisely the bias that a fixed map cannot, which is the mechanism the dual-timescale design was built to provide. Per-step cost is 0.33–0.42 ms, well within a 1 s BMS step.

Table 1. Labeled synthetic closed-loop SOC RMSE (Monte-Carlo mean ± std, %), convergence time and per-step cost.

Scenario	Dual-timescale (proposed)	Fixed magnitude	No hysteresis	Same-model EKF

Nominal	0.19 ± 0.07	0.07 ± 0.02	1.52 ± 0.08	0.35 ± 0.12
+30% magnitude drift	0.58 ± 0.06	2.47 ± 0.05 (no convergence)	2.79 ± 0.17	3.71 ± 1.20 (no convergence)

4.4 Sensitivity to representative power parameters and to capacity

Because the coin cell has no HPPC test, its RC power parameters are representative values. A Monte-Carlo sensitivity analysis therefore deliberately mismatches the filter's R0, combined R1+R2, time constants and capacity relative to the truth by factors of 0.5 to 1.5 (eight realizations each); Figure 4 reports the resulting SOC RMSE. Across ±50% mismatch in R0, R1+R2 or the time constants, the proposed dual-timescale filter remains within 0.14–0.57% and its curve is essentially flat, whereas the EKF rises to 3.39% when R0 is under-estimated by half and to 5.13% when the time constants are over-estimated by half, and the no-hysteresis filter reaches 6.70–7.66% under time-constant mismatch. The comparative ranking is therefore invariant to the precise choice of the representative power parameters, which directly addresses the absence of an HPPC characterization: only the correct order of the resistance is required, and that order is supplied by the DCIR measurement. Capacity behaves differently. A ±25–50% capacity error degrades every method, including the proposed one (17% at half capacity), because capacity sets the coulomb-counting rate that no amount of voltage correction can recover. This is stated as an explicit boundary of the method: capacity must be measured independently, and in the present work it is, from the genuine 145 mAh/g coin-cell capacity and from net coulomb counting on the public cells.

4.5 External validation on sloped-OCV NMC

Figure 5 shows the DST identification fit together with the six-profile RMSE comparison, while Table 2 reports the numerical values. Averaged over the six cases, the proposed filter reaches 1.01% RMSE with every maximum error at or below 2.80% and a convergence time near 300 s from a 15-point initial offset; the fixed-magnitude filter averages 1.25% and the EKF 3.70%. The EKF weakness is concentrated at the 50% initial-SOC starts, where it reaches 8.44% (US06) and 8.45% (BJDST) with maximum errors of 10.7% and convergence times above 6000 s. The slow magnitude state gives the proposed filter its consistent advantage on the profiles and initializations that the fixed-map filter handles poorly, without any chemistry-specific retuning of the filter structure.

Table 2. SOC RMSE / maximum absolute error (%) and convergence time (s) on six unseen CALCE NMC profiles.

Profile (initial SOC)	**Proposed RMSE / max / conv**	**Fixed RMSE / max**	**EKF RMSE / max / conv**
FUDS (80%)	1.12 / 2.79 / 304	0.98 / 1.59	0.22 / 1.76 / 304
FUDS (50%)	0.76 / 2.23 / 343	1.47 / 2.58	2.37 / 3.48 / 4809
US06 (80%)	0.82 / 2.75 / 304	1.27 / 5.57	1.38 / 2.75 / 304
US06 (50%)	0.84 / 2.80 / 302	1.34 / 5.77	8.44 / 10.74 / 6284
BJDST (80%)	0.96 / 2.69 / 302	1.14 / 5.46	1.35 / 2.69 / 302
BJDST (50%)	1.53 / 2.79 / 304	1.31 / 4.01	8.45 / 10.07 / 6539
Mean RMSE	**1.01**	**1.25**	**3.70**

4.6 External validation on flat-OCV LiFePO4 at three temperatures

Figure 6 first shows why this chemistry is demanding: the OCV is flat over a wide plateau whereas the measured charge/discharge hysteresis half-width is only 25–32 mV, which is already absorbed into the quasi-static OCV (the model therefore adopts zero explicit hysteresis). Figure 7 presents the SOC-error trajectories and Table 3 the numerical values, which together test numerical robustness where dOCV/dz is close to zero. The proposed filter remains accurate at every temperature: 0.40–2.16% RMSE with all maximum errors at or below 2.82%, and it converges from the 15-point initial offset within roughly five to six minutes. The same-model EKF degrades severely, to 4.85–12.49% RMSE with a worst-case maximum error of 20.63% at 50 °C, and its convergence stretches to 6945–7329 s at 25 °C. On the flat plateau the EKF measurement Jacobian is near zero, its voltage correction gain is effectively exhausted, and it cannot pull a wrong initial SOC back; the deterministic sigma points of the central-difference transform still sense the curvature at the edges of the plateau and the square-root covariance update remains well conditioned, so convergence is retained. The temperature dependence of the independently identified parameters is physically consistent: capacity decreases (1.055 Ah at 50 °C to 0.942 Ah at 0 °C) and ohmic resistance increases (0.1525 to 0.194 Ω) as temperature falls, yet the same filter settings generalize across all three temperatures without retuning. Because the LFP hysteresis is only 25–32 mV and is absorbed into the quasi-static OCV, this result evidences numerical robustness on a flat OCV rather than a hysteresis benefit; the two chemistries together show that the method is advantageous for distinct reasons—hysteresis compensation on the strong-hysteresis material and observability robustness on the flat-OCV chemistry.

Table 3. SOC RMSE / maximum error (%) of the proposed filter versus the EKF on CALCE A123 LiFePO4 at three temperatures (self-consistent capacity and DST identification at each temperature).

Temperature	Q (Ah) / R0 (Ω)	US06 proposed	US06 EKF	FUDS proposed	FUDS EKF
0 °C	0.942 / 0.194	1.31 / 2.06	6.96 / 8.50	0.40 / 1.17	6.49 / 9.00
25 °C	1.036 / 0.157	0.94 / 1.53	5.24 / 12.14	1.70 / 2.82	4.85 / 11.72
50 °C	1.055 / 0.1525	0.42 / 0.81	5.08 / 12.32	2.16 / 2.73	12.49 / 20.63

5. Discussion

5.1 Origin of the dual-timescale advantage

The results across all three evidence levels tell a consistent story about *which* part of the estimator matters and when. The fast direction state and the slow magnitude state solve different problems. The direction state removes the instantaneous branch ambiguity that, left untreated, gives the no-hysteresis filter its 1.5–2.8% floor; the slow magnitude state becomes valuable only when the identified map no longer matches the cell, whether because of an imposed drift in the synthetic test or because of the profile- and initialization-dependent bias visible in the fixed-magnitude NMC results. When the map happens to be exactly correct (the nominal synthetic row), a fixed-magnitude filter can be marginally more accurate because it estimates one fewer state; the dual-timescale design costs almost nothing in that case (0.19% versus 0.07%) but

becomes markedly superior as soon as any mismatch appears. This is the expected and desirable behaviour of an estimator intended for a vehicle, where the calibration map and the aged, temperature-dependent cell never coincide exactly.

5.2 Two distinct failure modes, one estimator

Placing a sloped-OCV NMC and a flat-OCV LiFePO4 side by side separates two failure modes that are often conflated. On NMC the challenge is mild hysteresis combined with ordinary nonlinearity, and a well-tuned EKF is adequate on easy starts; on LiFePO4 the challenge is weak voltage observability over a wide plateau, where the EKF Jacobian approaches zero and its correction gain is exhausted, producing the 5–12% errors and multi-hour convergence times in Table 3. The central-difference transform does not rely on a local derivative, and its square-root covariance update cannot lose positive-definiteness; these two properties, not the hysteresis model, are what keep the proposed filter accurate on LiFePO4. Conversely, on the strongly hysteretic coin cell the dominant benefit is the explicit, slowly adaptive hysteresis term, since a single-valued OCV would be biased by up to 0.46 V. Configuring the explicit hysteresis gain according to the chemistry—setting it to zero for the 25–32 mV LFP separation already absorbed into the quasi-static OCV—avoids over-claiming a single mechanism and shows that the framework degrades gracefully rather than requiring hysteresis to be large.

5.3 Evidence architecture under sparse characterization

A practical concern is that the strongly hysteretic material is available only as low-rate coin-cell data, with no dynamic schedule. The three-level architecture is designed around exactly this constraint and is worth making explicit. Low-rate GCD is the standard quasi-OCV measurement, so the coin cells legitimately supply the quantities that low-rate tests measure well—OCV shape, hysteresis width and reversible capacity; reviewers do not require a coin cell to execute a US06 schedule. Dynamic and power behaviour, which a coin cell cannot provide, are supplied by independent public cells on standard automotive schedules, and the ohmic-resistance *order* of the coin model is anchored by the genuine 0.1C/1C DCIR gap (18.5 Ω versus the adopted 20 Ω). The remaining representative RC values are then shown by the Monte-Carlo study to be non-critical: the method ranking is unchanged under ±50% errors in R0, the RC resistances and the time constants. The one parameter that must be exact, capacity, is the one that is genuinely measured. This division of labour closes the apparent gap between sparse material data and a credible dynamic-validation claim without presenting any unperformed dynamic experiment as measured.

5.4 Computational feasibility

The augmented state has five dimensions and therefore eleven sigma points; the measured per-step cost of 0.33–0.42 ms in a numerical scripting environment on a general-purpose processor indicates substantial head-room relative to a typical 10–100 ms BMS interval, and the QR-based square-root recursion avoids the matrix square roots or repeated Cholesky factorizations that would otherwise burden an embedded implementation. The algorithm is therefore compatible with real-time deployment, consistent with prior reports that sigma-point SOC filters are practical on automotive hardware [8,9].

5.5 Limitations

Several limitations bound the scope and define future work. The strongly hysteretic coin cell supplied only low-rate, quasi-static curves; its RC polarization parameters are representative values whose exact identification would require pulse tests, and the present work compensates for this by DCIR order-anchoring and an explicit sensitivity bound rather than by additional measurement. The synthetic closed-loop test is a simulation and is labeled as such; it isolates mechanism but is not experimental evidence, which is why the public NMC and LiFePO4 data carry the validation burden. The slow magnitude state is demonstrated over single-schedule and imposed-drift horizons, whereas validation over a full ageing trajectory, ideally jointly with state-of-health, remains future work. Finally, the strongest validation would be a dynamic schedule measured directly on a packaged strongly hysteretic lithium-rich/conversion cell; the present cross-chemistry public-data strategy is a rigorous substitute but not an equivalent of such a test. These boundaries are stated so that the evidence each result rests on is unambiguous.

6. Conclusion

This paper presented a SOC estimator that pairs a second-order equivalent circuit model with a dual-timescale hysteresis description—a fast current-weighted direction state plus a slow, sign-preserving magnitude-correction state—and embeds it in a square-root central difference Kalman filter. On a genuine strongly hysteretic lithium-rich/MnO@C coin cell, digitized low-rate curves establish a 0.457 V charge/discharge separation and a two-rate DCIR measurement anchors the model resistance at the correct order; a labeled synthetic test shows that an unknown +30% hysteresis-magnitude drift is held to 0.58% SOC error where fixed-magnitude and EKF baselines diverge; and on public CALCE cells the method reaches 1.01% mean error over six unseen NMC profiles and 0.40–2.16% over flat-OCV LiFePO4 profiles at 0, 25 and 50 °C, against 3.70% and 4.85–12.49% for a same-model EKF. A Monte-Carlo analysis proves the comparison robust to ±50% errors in the representative power parameters while identifying capacity as the single quantity that must be measured independently. At 0.3–0.4 ms per step the estimator is real-time feasible. The central conclusion is that separating fast hysteresis direction from slow magnitude drift, together with Jacobian-free, covariance-preserving sigma-point propagation, gives one estimator that is accurate both where OCV is strongly path dependent and where OCV is almost flat—a combination that is increasingly relevant as high-energy, strongly hysteretic chemistries move toward vehicle applications.

Statements and Declarations

Funding. This research received no specific grant from any funding agency in the public, commercial or not-for-profit sectors.

Competing interests. The author declares no competing interests.

Data availability. The public dynamic data are from the CALCE Battery Research Group, University of Maryland (https://calce.umd.edu/battery-data). The digitized coin-cell curves, the identified parameters, the

labeled synthetic test and the analysis scripts are available from the corresponding author upon reasonable request.

Author contributions. As the sole author, K.W. conceived the study, performed the digitization, modeling, computation and validation, and wrote the manuscript.

Use of generative AI. During the preparation of this work the author used Doubao (ByteDance Ltd.) as an assistant for cross-checking reference metadata, implementing numerical scripts and polishing language. The author independently designed the research, generated and verified every numerical result, critically revised the content, and takes full responsibility for the published article.

References

1. How DNT, Hannan MA, Lipu MSH, Ker PJ (2019) State of charge estimation for lithium-ion batteries using model-based and data-driven methods: A review. IEEE Access 7:136116–136136. https://doi.org/10.1109/ACCESS.2019.2942213

2. Wang Y, Tian J, Sun Z, Wang L, Xu R, Li M, Chen Z (2020) A comprehensive review of battery modeling and state estimation approaches for advanced battery management systems. Renew Sustain Energy Rev 131:110015. https://doi.org/10.1016/j.rser.2020.110015

3. Lai X, Zheng Y, Sun T (2018) A comparative study of different equivalent circuit models for estimating state-of-charge of lithium-ion batteries. Electrochim Acta 259:566–577. https://doi.org/10.1016/j.electacta.2017.10.153

4. Bian C, He H, Yang S (2020) Stacked bidirectional long short-term memory networks for state-of-charge estimation of lithium-ion batteries. Energy 191:116538. https://doi.org/10.1016/j.energy.2019.116538

5. Nejad S, Gladwin DT, Stone DA (2016) A systematic review of lumped-parameter equivalent circuit models for real-time estimation of lithium-ion battery states. J Power Sources 316:183–196. https://doi.org/10.1016/j.jpowsour.2016.03.042

6. Plett GL (2004) Extended Kalman filtering for battery management systems of LiPB-based HEV battery packs: Part 2. Modeling and identification. J Power Sources 134:262–276. https://doi.org/10.1016/j.jpowsour.2004.02.032

7. Plett GL (2006) Sigma-point Kalman filtering for battery management systems of LiPB-based HEV battery packs. J Power Sources 161:1369–1384. https://doi.org/10.1016/j.jpowsour.2006.06.004

8. Xuan D-J, Shi Z, Chen J, Zhang C, Wang Y-X (2020) Real-time estimation of state-of-charge in lithium-ion batteries using improved central difference transform method. J Clean Prod 252:119787. https://doi.org/10.1016/j.jclepro.2019.119787

9. Rezaei O, Habibifar R, Wang Z (2022) A robust Kalman filter-based approach for SoC estimation of lithium-ion batteries in smart homes. Energies 15:3768. https://doi.org/10.3390/en15103768

10. Assat G, Foix D, Delacourt C, Iadecola A, Dedryvère R, Tarascon J-M (2017) Fundamental interplay between anionic/cationic redox governing the kinetics and thermodynamics of lithium-rich cathodes. Nat Commun 8:2219. https://doi.org/10.1038/s41467-017-02291-9

11. Huang J, Ouyang B, Zhang Y, Yin L, Kwon D, Cai Z, Lun Z, Zeng G, Balasubramanian M, Ceder G (2023) Inhibiting collective cation migration in Li-rich cathode materials as a strategy to mitigate voltage hysteresis. Nat Mater 22:353–361. https://doi.org/10.1038/s41563-022-01467-z

12. Zhong K, Xia X, Zhang B, Li H, Wang Z, Chen L (2010) MnO powder as anode active materials for lithium ion batteries. J Power Sources 195:3300–3308. https://doi.org/10.1016/j.jpowsour.2009.11.133

13. Jahn L, Möhle P, Röder F, Danzer MA (2024) A physically motivated voltage hysteresis model for lithium-ion batteries using a probability distributed equivalent circuit. Commun Eng 3. https://doi.org/10.1038/s44172-024-00221-4

14. Huang K, Sun K, Guo Y, Wang Z, Li S (2023) Battery modeling considering hysteresis effect and temperature adaptability. Energy Technol 11. https://doi.org/10.1002/ente.202201064

15. Yang F, Xing Y, Wang D, Tsui K-L (2016) A comparative study of three model-based algorithms for estimating state-of-charge of lithium-ion batteries under a new combined dynamic loading profile. Appl Energy 164:387–399. https://doi.org/10.1016/j.apenergy.2015.11.072

16. Yu Q, Xiong R, Lin C, Shen W, Deng J (2017) Lithium-ion battery parameters and state-of-charge joint estimation based on H-infinity and unscented Kalman filters. IEEE Trans Veh Technol 66:8693–8701. https://doi.org/10.1109/TVT.2017.2709326

17. Xing Y, He W, Pecht M, Tsui K-L (2014) State of charge estimation of lithium-ion batteries using the open-circuit voltage at various ambient temperatures. Appl Energy 113:106–115. https://doi.org/10.1016/j.apenergy.2013.07.008

18. He W, Williard N, Chen C, Pecht M (2014) State of charge estimation for Li-ion batteries using neural network modeling and unscented Kalman filter-based error cancellation. Int J Electr Power Energy Syst 62:783–791. https://doi.org/10.1016/j.ijepes.2014.04.059

19. Zhong K, Zhang B, Luo S, Wen W, Li H, Huang X, Chen L (2011) Investigation on porous MnO microsphere anode for lithium ion batteries. J Power Sources 196:6802–6808. https://doi.org/10.1016/j.jpowsour.2010.10.031

Figure captions

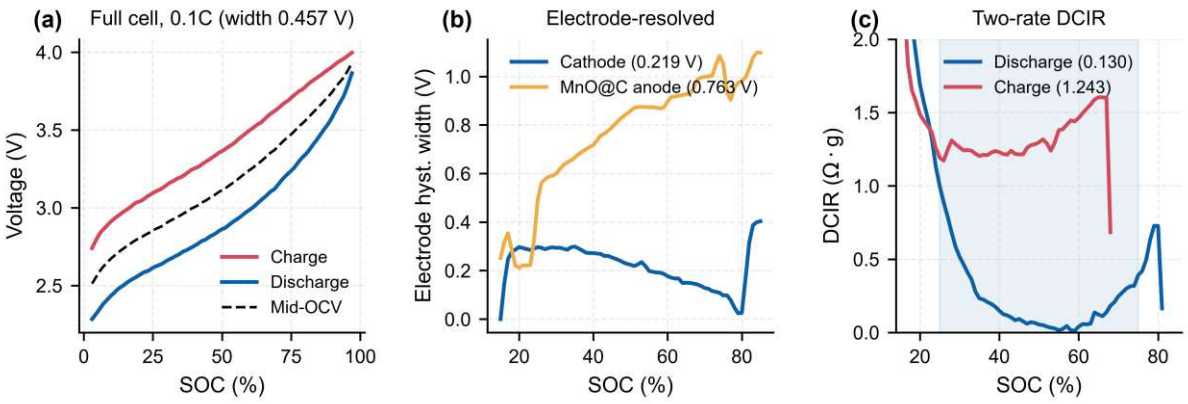


Fig. 1 Digitized genuine coin-cell characteristics. (a) Charge, discharge and mid-OCV curves of the lithium-rich/MnO@C full cell (0.1C, mean 0.457 V hysteresis width); (b) electrode-resolved hysteresis of the lithium-rich cathode (mean 0.219 V) and MnO@C anode (mean 0.763 V); (c) two-rate (0.1C versus 1C) discharge/charge DCIR, with the 25–75% SOC evaluation window shaded (medians 0.130 and 1.243 Ω·g)

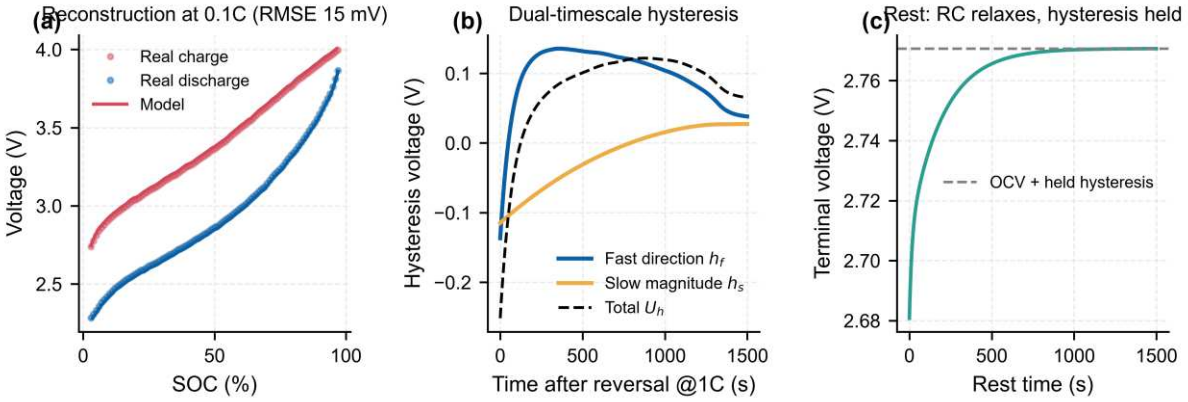


Fig. 2 Open-loop verification of the dual-timescale model on the genuine cell. (a) 0.1C charge/discharge reconstruction (RMSE 15 mV); (b) fast direction state, slow magnitude state and their total after a current reversal; (c) terminal-voltage relaxation during rest, where RC polarization decays while hysteresis is held

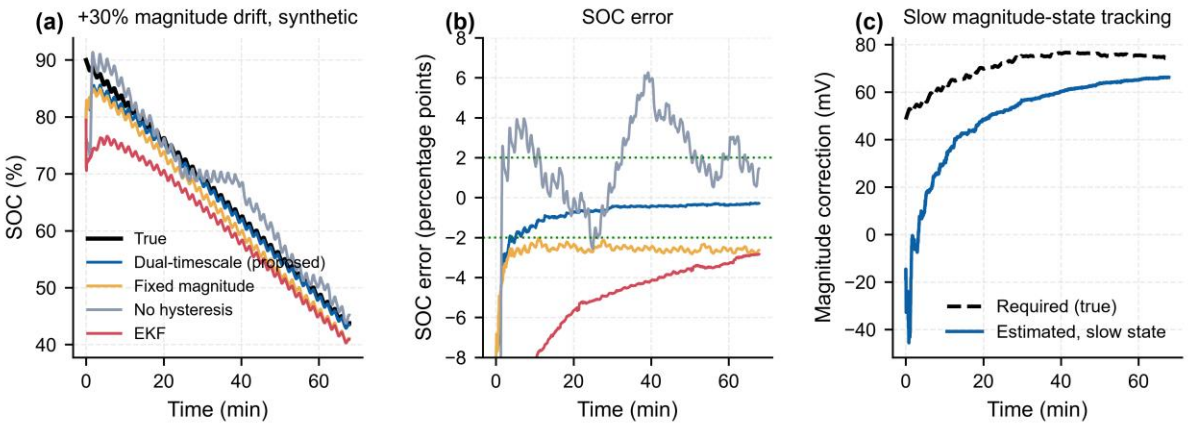


Fig. 3 Labeled synthetic closed-loop test under a +30% hysteresis-magnitude drift (simulation). (a) SOC trajectories; (b) SOC errors with the ±2% band; (c) tracking of the required magnitude correction by the slow state

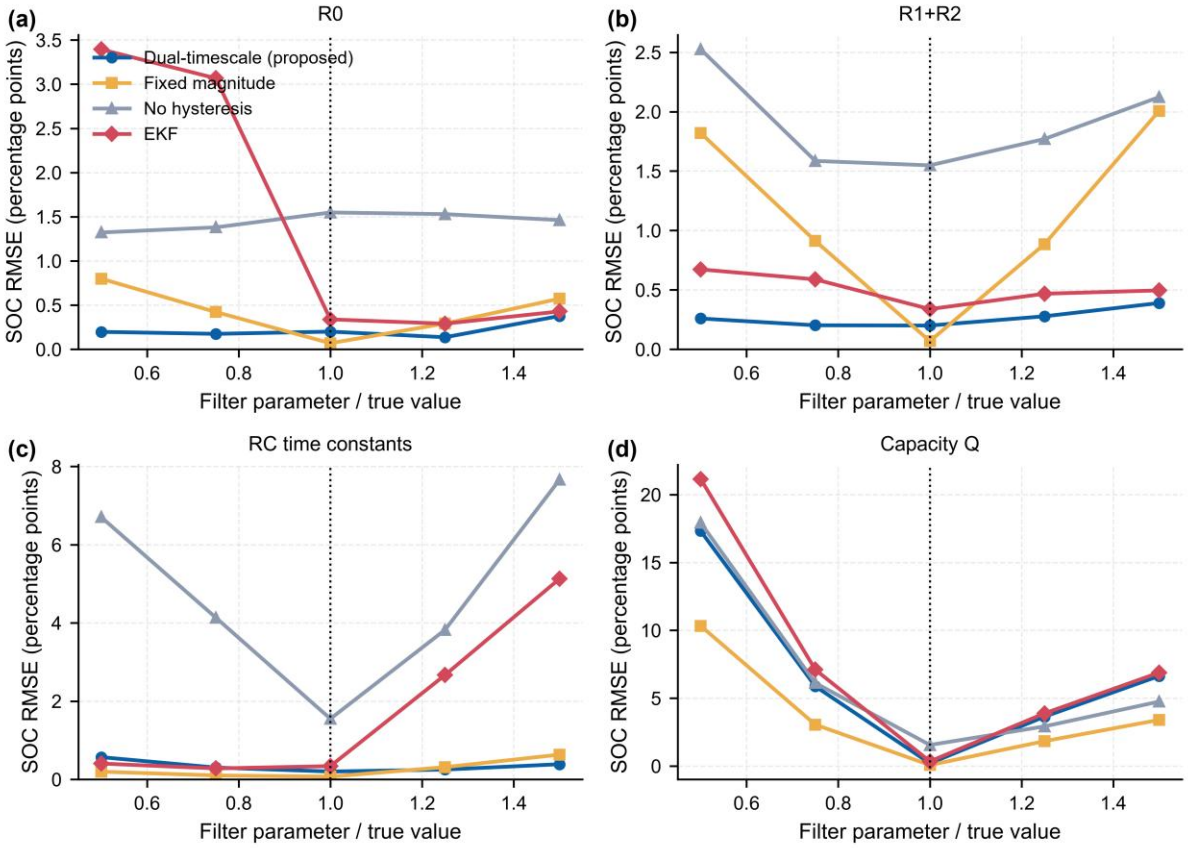


Fig. 4 Monte-Carlo sensitivity of SOC RMSE to deliberate 0.5–1.5× mismatch in (a) R0, (b) R1+R2, (c) RC time constants and (d) capacity (synthetic, eight realizations per point). The proposed filter is flat under power-parameter mismatch; all methods require an independently measured capacity

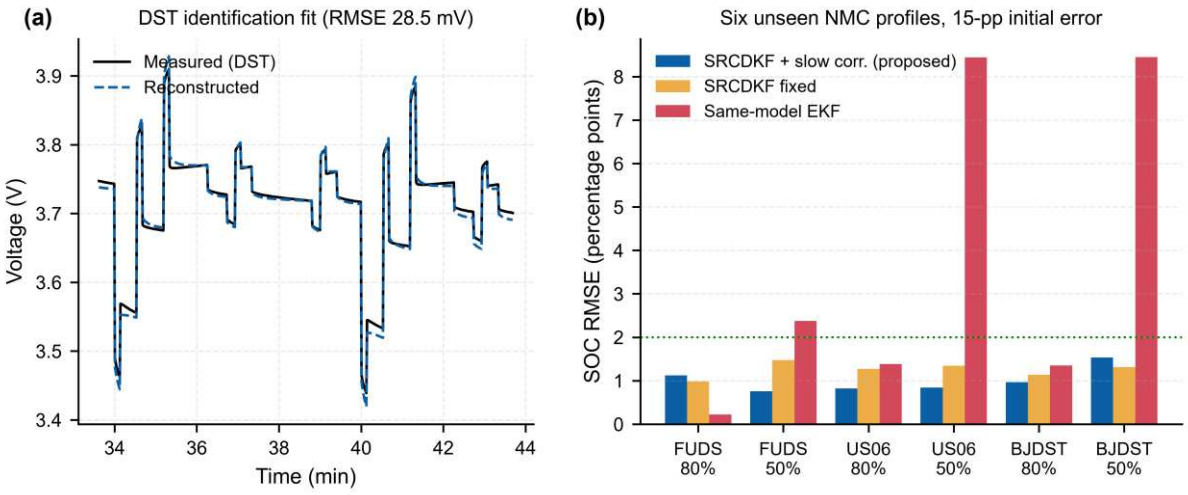


Fig. 5 External validation on CALCE NMC (INR18650-20R). (a) DST identification fit of measured versus reconstructed voltage (RMSE 28.5 mV); (b) SOC RMSE on six unseen FUDS/US06/BJDST profiles started 15 percentage points off

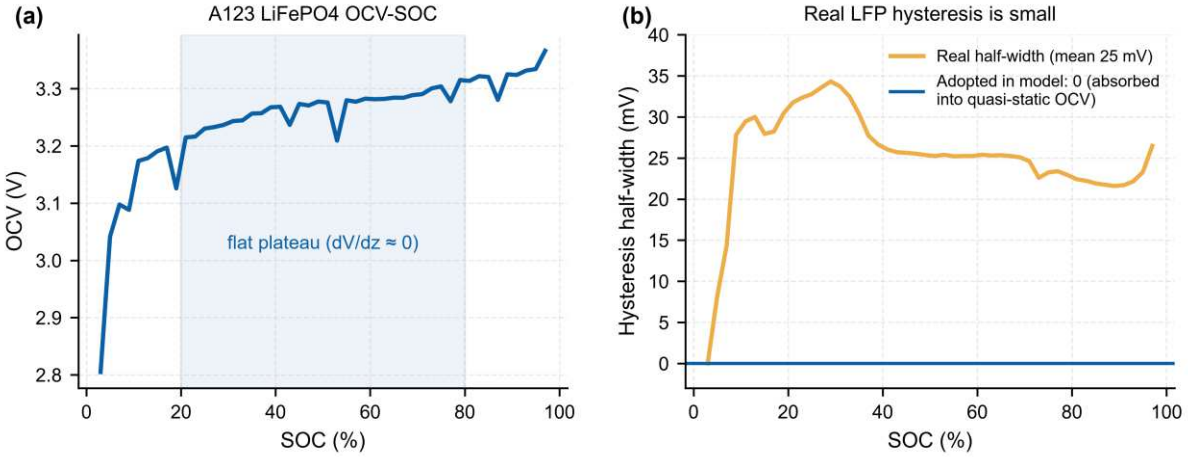


Fig. 6 Why the LiFePO4 chemistry is demanding. (a) Flat A123 OCV-SOC plateau (dV/dz ≈ 0 over the shaded range); (b) measured hysteresis half-width (mean 25 mV) versus the zero explicit hysteresis adopted after its absorption into the quasi-static OCV

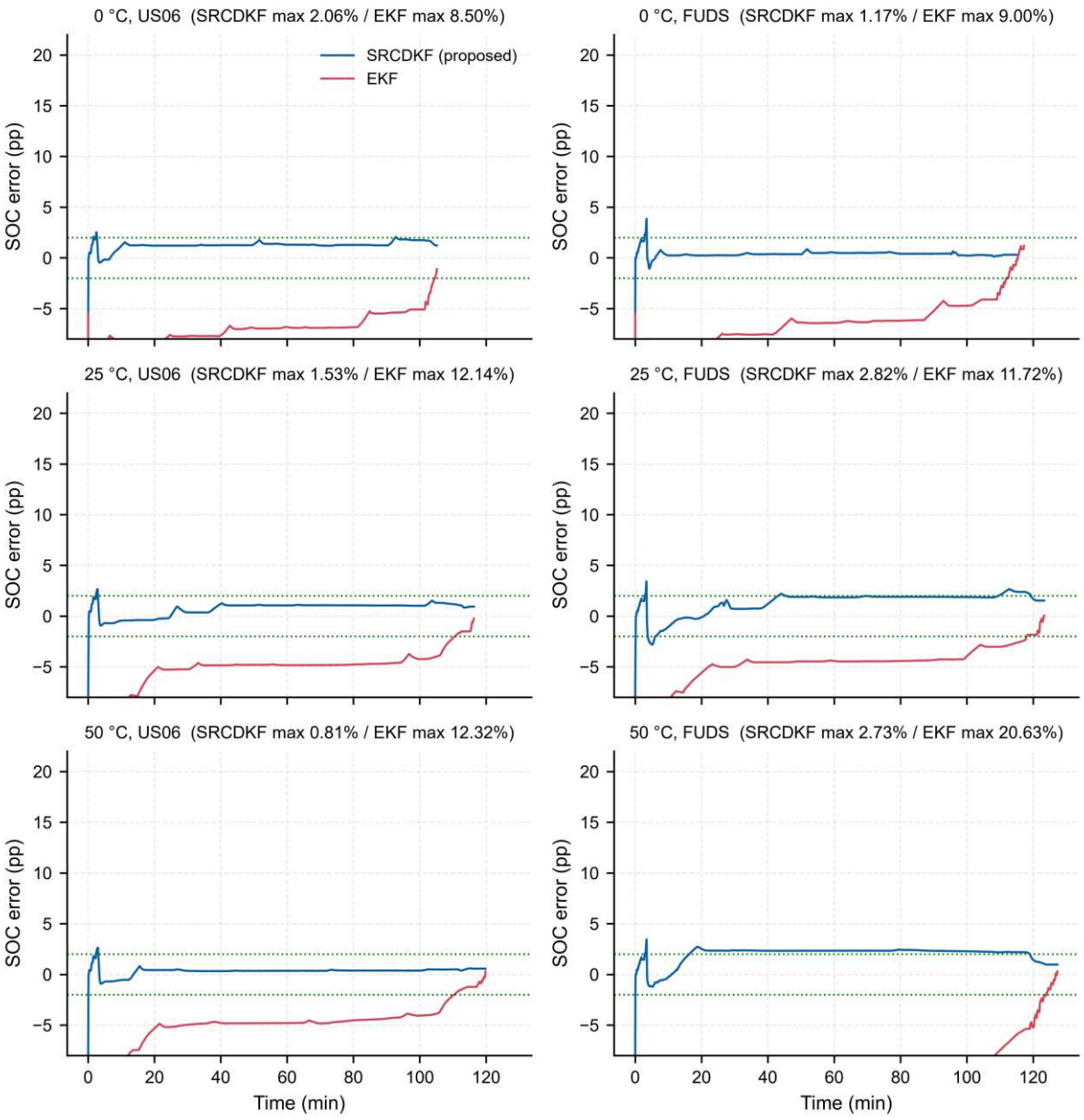


Fig. 7 CALCE A123 LiFePO4 at 0, 25 and 50 °C: SOC-error trajectories of the proposed SRCDKF versus the same-model EKF from a 15-point initial SOC error on the flat OCV plateau (US06 and FUDS columns; dotted lines mark ±2%)

Supplementary Files

This is a list of supplementary files associated with this preprint. Click to download.

- ESM1SupplementaryInformation.docx